Voltage Support Provided by Three-Phase Three-Wire Inverters With Independent Reactive Phase-Current Injection

José Ignacio Iñiguez, Josué Neftali Duarte, Antonio Camacho, Jaume Miret, *Member, IEEE*, and Miguel Castilla

***Abstract*—During voltage sags, three-phase three-wire power inverters can provide voltage support with several current injection strategies. In general, good results are obtained, except in overvoltage situations when one or more phase voltages exceed the allowed limit in grid codes. In three-wire inverters, this is a challenging problem because phase voltages are coupled. In this article, we present a strategy that performs independent reactive current injection for each phase, which solves the overvoltage problem. This approach also includes a current-limiting technique that guarantees the injection of the maximum active power under safe current conditions. A stability analysis is carried out based on the small-gain theorem. The properties of the proposed control are experimentally validated with selected tests in a laboratory setup. A performance comparison with state-of-the-art control strategies is also included in the experimental validation.**

***Index Terms*—Grid code, reactive current injection, three-phase power inverter, voltage sags, voltage support.**

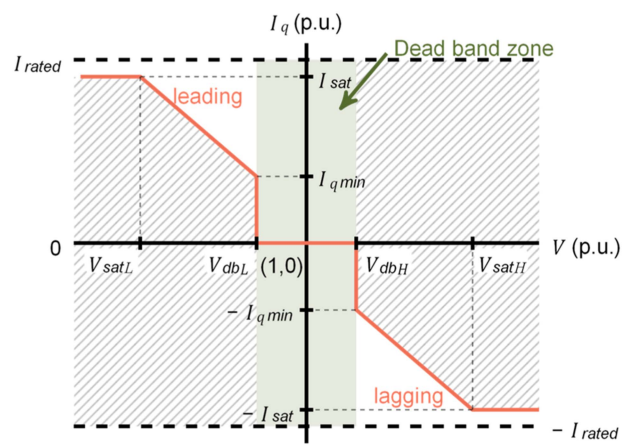

Fig. 1. Generic representative illustration of reactive current injection in grid codes.

I. Introduction

VOLTAGE sags are the largest disturbances found in power systems [1]. They are produced by short circuits and usually cause voltage imbalances throughout the grid [2], [3]. Dedicated power converters, such as flexible alternative-current transmission (FACT) systems [4], [5] or active power filters [6], [7], can be used to overcome voltage problems during voltage sags with very satisfactory results. With them, it is possible to correct voltage imbalances by removing the negative-sequence voltage. The main drawback of this solution is the high cost of using power converters dedicated exclusively to improve power quality. An alternative option to alleviate the negative impact of voltage sags is to use distributed generators (DGs) [8], [9], [10]. The main function of DG systems is to export the generated power to the main grid. With the remaining power capacity, DG systems can perform auxiliary functions, such as voltage support. As the power capacity available for auxiliary functions is normally limited, the improvement reached with this solution is smaller than those obtained with dedicated power converters [11], [12]. In the case of voltage support, the negative-sequence voltage is rarely removed and only reductions on this component are expected [13], [14], [15]. However, the cost of this solution is very low, which makes it a very attractive option today.

The operation of DG power inverters during voltage sags is defined by grid codes [16], [17]. In particular, inverters must inject reactive current to support the grid voltage according to the voltage measured at the point-of-common coupling (PCC). Fig. 1 shows a generic representation of the reactive current injection specified in grid codes [17]. Normal operation is marked as a dead band zone and corresponds to the voltage interval $V_{\mathrm{dbL}} < V < V_{\mathrm{dbH}}$. The nominal voltage $V = 1$ p.u. lies at the center of this interval. Note that the reactive current injection is not necessary in this zone ($I_q = 0$) [18]. Below the lower dead

Manuscript received 2 August 2023; revised 16 November 2023; accepted 22 December 2023. Date of publication 19 January 2024; date of current version 19 June 2024. This work was supported in part by MCIN/AEI/10.13039/501000011 033 and in part by FEDER "Una manera de hacer Europa" under Project PID2021-122835OB-C21. *(Corresponding author: Miguel Castilla.)*

José Ignacio Iñiguez, Jaume Miret, and Miguel Castilla are with the Department of Electronic Engineering, Universitat Politècnica de Catalunya, 08800 Vilanova i la Geltrú, Spain (e-mail: jose.ignacio.iniguez@upc.edu; jaume.miret@upc.edu; miquel.castilla@upc.edu).

Josué Neftali Duarte and Antonio Camacho are with the Department of Automatic Control, Universitat Politècnica de Catalunya, 08028 Barcelona, Spain (e-mail: josue.duarte@upc.edu; antonio.camacho.santiago@upc.edu).

Color versions of one or more figures in this article are available at https://doi.org/10.1109/TIE.2024.3349525.

Digital Object Identifier 10.1109/TIE.2024.3349525

© 2024 The Authors. This work is licensed under a Creative Commons Attribution 4.0 License. For more information, see http://creativecommons.org/licenses/by/4.0/

TABLE I
CURRENT INJECTION STRATEGIES USING DIFFERENT INTERPRETATION OF THE CURRENT- AND VOLTAGE-AXIS MEANINGS IN FIG. 1

Strategy	Grid code	Current axis in Fig. 1 (I_q)	Voltage axis in Fig. 1 (V)	Voltage meaning	Ref.
1	$I_q^+ = f(V^+)$	reactive positive-sequence current amplitude	positive-sequence voltage amplitude	V^+	[27], [28], [29], [30], [31], [32], [33], [34], [35], [36], [37]
2	$I_q^+ = f(V_{ag})$	reactive positive-sequence current amplitude	aggregate voltage	$V_{ag} = (V_a + V_b + V_c)/3$	[25], [38]
3	$I_q^+ = f(V_{ef})$	reactive positive-sequence current amplitude	effective voltage	$V_{ef} = \sqrt{(V^+)^2 + (V^-)^2}$	[23], [24]
4	$I_q^+ = f(V_{min})$	reactive positive-sequence current amplitude	minimum phase-voltage amplitude	$V_{min} = \min(V_a, V_b, V_c)$	[26], [39]
5	$I_{qx} = f(V_x)$	reactive phase-current amplitude ($x = a, b, c$)	phase-voltage amplitude ($x = a, b, c$)	V_a, V_b, V_c	[40]

band V_{dbL}, the inverter must inject a reactive current to increase the PCC voltage. In the zone $V_{\text{satL}} < V < V_{\text{dbL}}$, the current is proportional to the voltage. For deep disturbances ($V < V_{\text{satL}}$), the reactive current requirement saturates $I_q = I_{\text{sat}}$ at a level close to the rated current I_{rated} [19], [20]. Above the higher dead band V_{dbH}, the inverter must absorb reactive current (see the negative signs in Fig. 1) to decrease the PCC voltage [21], [22]. The figure shows a zone with reactive current proportional to the voltage and another with saturated current [23], [24].

Several current injection strategies have been developed in the literature according to the generic grid-code specification, as shown in Fig. 1; see the reviews [25], [26]. These strategies respond to a different interpretation of the meaning of the current and voltage axis in Fig. 1. Table I lists them, including the definition of the currents and voltages involved. The first four strategies inject a reactive positive-sequence current (I_q^+) as a function of a slightly different voltage [23], [24], [25], [26], [27], [28], [29], [30], [31], [32], [33], [34], [35], [36], [37], [38], [39]; see Table I. The strategies consider these particular voltages to test compliance with the curve in Fig. 1. In these strategies, good results are obtained for voltage support, especially when the negative-sequence voltage is low. However, an overvoltage problem has been observed when the negative-sequence voltage is high. In this case, the amplitudes of the phase voltages are markedly different. Even, in some cases, some phase voltages may be above the V_{dbH} limit, causing an overvoltage problem [40]. This problem is easily solved in three-phase four-wire power inverters in which phase voltages are decoupled. Therefore, reactive current injection can be independently performed for each phase, emulating the operation of a single-phase control [41]. The problem is really challenging in three-phase three-wire inverters, which have coupled phase voltages. For these systems, the main limitation of the considered strategies is that they have a single control input (I_q^+) for voltage support. Therefore, they are not optimized to simultaneously increase the phase voltages with amplitudes lower than V_{dbL} and decrease the phase voltages with amplitudes higher than V_{dbH}, as desired in practice. The last strategy in Table I is devised to solve this problem in three-phase three-wire inverters [40]. It considers the injection of reactive current independently for each phase, denoting the use of three independent control inputs for voltage support (I_{qa}, I_{qb}, and I_{qc}). Consequently, it seems the best solution since it provides the appropriate reactive current per phase according to the voltage of each phase. Therefore, if the voltage of one phase exceeds V_{dbH}, its reactive phase current will be negative, reducing this phase voltage. If the voltage of one phase is below

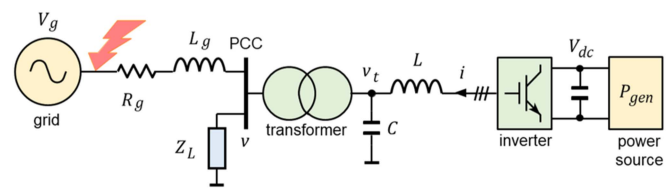

Fig. 2. Grid-connected three-phase three-wire inverter with local load.

V_{dbL}, its reactive phase current will be positive, increasing this phase voltage. Even if one phase voltage is in normal operation (inside the dead band zone), its reactive phase current is zero, thus not participating in the voltage support. However, the control implementation of this strategy in [40] does not work correctly when the current limiting is activated. In fact, this control uses two current-limiting mechanisms, the first one to prioritize the reactive current injection and the second one to eliminate the zero-sequence current in the three-phase three-wire inverter. When this last mechanism is activated, the reactive current requirements specified by the grid code in Fig. 1 are not met. For this reason, this implementation is not considered further in this work.

In this article, a control scheme is proposed to implement the reactive current injection strategy named 5 in Table I. The proposed implementation works correctly in all circumstances and provides better voltage support than the other strategies. The proposed control also includes a current-limiting technique that guarantees the injection of maximum active power under safe current conditions.

The rest of this article is organized as follows. In Section II, the problem is formulated mathematically. In Section III, the proposed solution is presented. In Section IV, the stability of the proposal is analyzed. In Section V, the proposed control is experimentally validated. Finally, Section VI concludes this article.

II. PROBLEM STATEMENT

In this section, the problem is written mathematically based on the necessary knowledge about the inverter and its control.

A. Grid-Connected Inverter

Fig. 2 shows the single-line diagram of a grid-connected inverter with a local load (Z_L). The grid is modeled as an unbalanced voltage source and a series grid impedance (R_g and

TASK: Controller(·)

1 /* Sampling and processing */
2 $(v_a, v_b, v_c, v_{ta}, v_{tb}, v_{tc}, i_a, i_b, i_c, V_{dc}) := \text{ReadADC}(\cdot)$
3 $(V_a, V_b, V_c) := \sqrt{2}\,\text{RMS}(v_a, v_b, v_c)$
4 $(I_a, I_b, I_c) := \sqrt{2}\,\text{RMS}(i_a, i_b, i_c)$
5 $(v_{t\alpha}, v_{t\beta}) := \text{Clarke}(v_{ta}, v_{tb}, v_{tc})$
6 $(i_\alpha, i_\beta) := \text{Clarke}(i_a, i_b, i_c)$
7 $(v_{t\alpha}^+, v_{t\beta}^+, v_{t\alpha}^-, v_{t\beta}^-) := \text{Sequence Extractor}(v_{t\alpha}, v_{t\beta})$ /* [42], [43] */
8 $(V_t^+, V_t^-, \cos\varphi, \sin\varphi) := \text{MagnitudAngle}(v_{t\alpha}^+, v_{t\beta}^+, v_{t\alpha}^-, v_{t\beta}^-)$ /* [39] */
9 /* Proposed control (external voltage control loop) */
10 $(I_{qa}, I_{qb}, I_{qc}) := \text{Grid Code}(V_a, V_b, V_c)$ /* (7) − (9) */
11 $P := \text{Current Limiting}(I_a, I_b, I_c, P_{gen})$ /* (11) */
12 $(I_p^+, I_q^+, I_p^-, I_q^-) := \text{Phase to Sequence Mapping}(I_{qa}, I_{qb}, I_{qc}, P)$ /* (16) − (19) */
13 $(i_\alpha^*, i_\beta^*) := \text{Current References}(v_{t\alpha}^+, v_{t\beta}^+, v_{t\alpha}^-, v_{t\beta}^-, I_p^+, I_q^+, I_p^-, I_q^-)$ /* (1), (2) */
14 /* Internal current control loop and modulator */
15 $(d_\alpha, d_\beta) := \text{PRES}(i_\alpha^* - i_\alpha, i_\beta^* - i_\beta)$ /* [44] */
16 $(T_a, T_b, T_c) := \text{Space Vector Modulation}(d_\alpha, d_\beta)$

Fig. 3. Pseudocode of the proposed control strategy.

L_g). The inverter is a three-phase three-wire topology, with an LC output filter and a power transformer. Its input is supplied from a DG power source. Both the grid and the inverter supply a local load. The figure also shows the inverter voltage v_t and current i, and the PCC voltage v. The phase components of these variables are denoted as v_{ta}, v_{tb}, and v_{tc} for the inverter voltages, i_a, i_b, and i_c for the inverter currents and, finally, v_a, v_b, and v_c for the PCC voltage.

Fig. 3 shows the pseudocode implementing the control task. This pseudocode includes comments to indicate both the equations of the proposed control and references where the standard code can be consulted. This way of presenting the control scheme allows for clearly identifying the inputs and outputs of the control functions as well as the equations that implement them. In Fig. 3, the first part is a standard code that is responsible for sensing and processing input data. It includes the measurement of voltages and currents in natural reference frame, the use of a root-mean-square (RMS) algorithm, the Clarke transformation, a sequence voltage extractor [42], [43], and an algorithm that obtains the amplitudes and angle of the sequence voltages [39]; see lines 2–8. The second part of the controller is the contribution of this article. It calculates the amplitude of the sequence currents (line 12) from the grid-code requirements (line 10) and the current-limiting technique (line 11). These sequence currents are the control signals of the external control loop responsible for voltage support. The last part of the controller implements the standard internal current control loop and modulator. In line 14, the current references are computed as [44]

$$i_\alpha^* = \frac{v_{t\alpha}^+}{V_t^+} I_p^+ + \frac{v_{t\beta}^+}{V_t^+} I_q^+ + \frac{v_{t\alpha}^-}{V_t^-} I_p^- + \frac{v_{t\beta}^-}{V_t^-} I_q^- \tag{1}$$

$$i_\beta^* = \frac{v_{t\beta}^+}{V_t^+} I_p^+ - \frac{v_{t\alpha}^+}{V_t^+} I_q^+ + \frac{v_{t\beta}^-}{V_t^-} I_p^- - \frac{v_{t\alpha}^-}{V_t^-} I_q^- . \tag{2}$$

In line 15, a proportional–resonant (PRES) compensator is used in the internal control loop to ensure that the injected currents follow their references [45]. Finally, in line 16, a space-vector pulsewidth modulator obtains the switching times of each inverter branch.

B. Problem Formulation

In this article, the problem to be solved is to find the phase to sequence mapping function in Fig. 3, line 12. In other words, to find the amplitudes of the sequence currents $(I_p^+, I_q^+, I_p^-, I_q^-)$ that guarantee the injection of both independent reactive phase currents (I_{qa}, I_{qb}, I_{qc}) and maximum active power (P), these control objectives must be obtained without exceeding the limit of the inverter maximum current (I_{rated}). Mathematically, the problem is formulated as

$$\text{find } I_p^+, I_q^+, I_p^-, I_q^- \tag{3}$$

$$\text{such that } I_{qa} = f(V_a),\ I_{qb} = f(V_b),\ I_{qc} = f(V_c) \tag{4}$$

$$P \le P_{\text{gen}} \tag{5}$$

$$\max(I_a, I_b, I_c) \le I_{\text{rated}} \tag{6}$$

where P_{gen} is the power generated by the power source; see Fig. 2.

It is worth mentioning that this problem has not been solved previously in the literature for three-phase three-wire inverters. Its solution provides excellent voltage support characteristics compared with state-of-the-art control solutions, as shown in Section V.

III. Proposed Control Solution

In this section, the three control functions that make up the contribution of this article are presented.

A. Reference Reactive Currents

This section develops the control function, as indicated in Fig. 3, line 10. To get independent reactive phase-current injection, the grid-code requirements, as shown in Fig. 1, are applied, as follows:

$$I_{qx} = \begin{cases} I_{\text{sat}} & 0 \le V_x < V_{\text{satL}} \\ s_L(V_x - V_{\text{satL}}) + I_{\text{sat}} & V_{\text{satL}} \le V_x < V_{\text{dbL}} \\ 0 & V_{\text{dbL}} \le V_x < V_{\text{dbH}} \\ s_H(V_x - V_{\text{satH}}) - I_{\text{sat}} & V_{\text{dbH}} \le V_x < V_{\text{satH}} \\ -I_{\text{sat}} & V_{\text{satH}} \le V_x \end{cases} \tag{7}$$

where the slopes are calculated as

$$s_L = \frac{I_{q\min} - I_{\text{sat}}}{V_{\text{dbL}} - V_{\text{satL}}} \tag{8}$$

$$s_H = \frac{I_{\text{sat}} - I_{q\min}}{V_{\text{dbH}} - V_{\text{satH}}} . \tag{9}$$

Note that all the variables in (7)–(9) were defined in Fig. 1.

Once the independent reactive current injection is proposed in (7)–(9), the merit factors for voltage support can be defined

TABLE II
EXPRESSIONS FOR ACTIVE AND REACTIVE (PHASE) POWERS

Quantity	Expression	Eq.
Active power	$P = \frac{3}{2}\left(V_t^+ I_p^+ + V_t^- I_p^-\right)$	(12)
Reactive (phase a) power	$\frac{1}{2}V_a I_{qa} = \frac{1}{2}\left(V_t^+ I_q^+ - V_t^- I_q^-\right) + \frac{3}{2}\left(-V_t^+ I_q^- + V_t^- I_q^+\right)\cos(\varphi) + \frac{3}{2}\left(V_t^+ I_p^- - V_t^- I_p^+\right)\sin(\varphi)$	(13)
Reactive (phase b) power	$\frac{1}{2}V_b I_{qb} = \frac{1}{2}\left(V_t^+ I_q^+ - V_t^- I_q^-\right) + \frac{3}{2}\left(-V_t^+ I_q^- + V_t^- I_q^+\right)\cos\left(\varphi + \frac{2\pi}{3}\right) + \frac{3}{2}\left(V_t^+ I_p^- - V_t^- I_p^+\right)\sin\left(\varphi + \frac{2\pi}{3}\right)$	(14)
Reactive (phase c) power	$\frac{1}{2}V_c I_{qc} = \frac{1}{2}\left(V_t^+ I_q^+ - V_t^- I_q^-\right) + \frac{3}{2}\left(-V_t^+ I_q^- + V_t^- I_q^+\right)\cos\left(\varphi - \frac{2\pi}{3}\right) + \frac{3}{2}\left(V_t^+ I_p^- - V_t^- I_p^+\right)\sin\left(\varphi - \frac{2\pi}{3}\right)$	(15)

for each phase as follows:

$$\Delta V_x = \begin{cases} V_x - V_{x,NI} & 0 \le V_x < V_{\text{dbL}} \\ \text{Not defined} & V_{\text{dbL}} \le V_x < V_{\text{dbH}} \\ V_{x,\,NI} - V_x & V_{\text{dbH}} \le V_x \end{cases} \tag{10}$$

where $V_{x,NI}$ is the measured voltage in phase x without reactive current injection. The definition in (10) takes into account that an improvement in voltage support produces a positive value of ΔV_x for both V_x lower than V_{dbL} and V_x higher than V_{dbH}. With this definition, it is easier to interpret the results produced by the injection of reactive current. It should be noted that the measurement of $V_{x,NI}$ is not necessary for the operation of the control proposed in this article; see Fig. 3. It is used only to quantify the improvement obtained, which must be carried out in two separate tests: the first one without reactive current injection and the second one with the specific reactive current injection.

B. Current-Limiting Technique

This section presents the control function, as indicated in Fig. 3, line 11, in accordance with the restrictions written in (5) and (6). This function ensures the safe operation of the inverter during overcurrent conditions. It is based on curtailing the generated power P_{gen} in case the maximum inverter current (I_{rated}) is exceeded. It is implemented as follows:

$$P = \min\left(P_{\text{gen}}, \frac{I_{\text{rated}}}{\max\left(I_a, I_b, I_c\right)} P\right). \tag{11}$$

It is worth noting that the protection of the inverter against fast transient phenomena is carried out with a standard function (not included in Fig. 3) that uses the instantaneous values of the currents. This fast protection mechanism is necessary since (11) depends on RMS calculations, which may require almost one grid cycle to be accurate. Another issue related to (11) is that the nonexported active power from the power source $P_{\text{gen}} - P$ must be evacuated with a dedicated mechanism; some examples can be found at [26], [27], and [46].

C. Reference Sequence Currents

This section shows the solution to the problem formulated in (3)–(6), resulting in the control function, as indicated in Fig. 3, line 12.

A three-phase three-wire inverter is a power converter that has four independent outputs and can be controlled with four independent control inputs [41]. In this article, since the inverter operates in grid-feeding mode [45], the outputs are the sequence currents (I_p^+, I_q^+, I_p^-, I_q^-) and the control inputs are the reactive phase currents and the active power (I_{qa}, I_{qb}, I_{qc}, P). To solve the problem formulated in (3), the first step is to obtain the expressions for the active and reactive powers. These expressions are derived in the Appendix and are shown in Table II. Note that (12)–(15) is a system of four equations and four unknowns (the sequence currents). The control inputs and the voltage sag characteristics (V_t^+, V_t^-, φ) are known quantities. Therefore, solving this system for the unknowns, the solution to (3) is written as

$$I_p^+ = \frac{2}{3}\,\frac{V_t^+ P - V_t^-\left(Q_\alpha \sin(\varphi) + Q_\beta \cos(\varphi)\right)}{\left(V_t^+\right)^2 + \left(V_t^-\right)^2} \tag{16}$$

$$I_q^+ = \frac{2}{3}\,\frac{V_t^+ Q - V_t^-\left(Q_\alpha \cos(\varphi) - Q_\beta \sin(\varphi)\right)}{\left(V_t^+\right)^2 - \left(V_t^-\right)^2} \tag{17}$$

$$I_p^- = \frac{2}{3}\,\frac{V_t^- P + V_t^+\left(Q_\alpha \sin(\varphi) + Q_\beta \cos(\varphi)\right)}{\left(V_t^+\right)^2 + \left(V_t^-\right)^2} \tag{18}$$

$$I_q^- = \frac{2}{3}\,\frac{V_t^- Q - V_t^+\left(Q_\alpha \cos(\varphi) - Q_\beta \sin(\varphi)\right)}{\left(V_t^+\right)^2 - \left(V_t^-\right)^2} \tag{19}$$

where

$$Q = \frac{1}{2}\left(V_a I_{qa} + V_b I_{qb} + V_c I_{qc}\right) \tag{20}$$

$$Q_\alpha = \frac{1}{2}\left(2V_a I_{qa} - V_b I_{qb} - V_c I_{qc}\right) \tag{21}$$

$$Q_\beta = \frac{\sqrt{3}}{2}\left(V_b I_{qb} - V_c I_{qc}\right). \tag{22}$$

Note that the current injection strategy proposed in (16)–(22) is independent of the grid (R_g and L_g) and load (Z_L) impedances. Therefore, the objectives expressed in (4)–(6) can be satisfactorily achieved for any value of these impedances. However, the improvement in voltage support is affected by changes in these impedances, as shown in Section V-C.

In normal operation ($V_{\text{dbL}} \le V_x < V_{\text{dbH}}$), no reactive power is injected, while active power is injected only through the positive-sequence component as follows:

$$I_p^+ = \frac{2}{3}\,\frac{P}{V_t^+} \tag{23}$$

$$I_q^+ = 0 \tag{24}$$

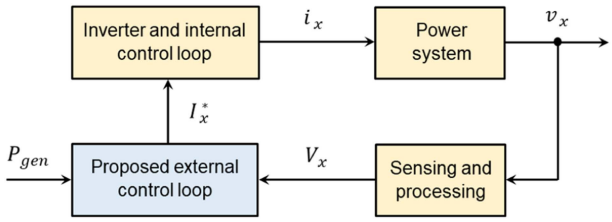

Fig. 4. Diagram of the closed-loop control system.

$$I_p^- = I_q^- = 0. \tag{25}$$

IV. Stability Analysis

Fig. 4 shows a diagram of the closed-loop control system. It includes three standard blocks and the proposed control block. The assumptions of this analysis are that the internal control loop has no tracking error and is stable. To achieve these features, this control loop must be designed correctly [45].

The stability of the proposed control loop is carried out using the small-gain theorem [47]. Based on the Nyquist criterion, it states that a sufficient condition for stability is that the gain of a signal passing through the loop is lower than 1 for all frequencies [48]. In Fig. 4, the sensing and processing block includes a sequence voltage extractor that behaves as a highly selective bandpass filter centered at the grid frequency ω_g [42], [43]. Due to the high attenuation introduced by this filter outside its passband, the highest loop gain is obtained at ω_g. Therefore, the worst condition for the stability analysis is derived at this frequency.

In Fig. 4, the gains of the blocks at ω_g are as follows. With a good enough tracking of the reference currents, the gain of the inverter and internal control loop is 1 [45]. Also, the gain in the sequence voltage extractor is 1 [43]. According to Fig. 2, the power system gain is the magnitude of the grid impedance [49]. Finally, the gain of the proposed control depends on the function expressed in (7)–(9), the current limitation in (11), and the sequence currents in (16)–(19). These three functions are nonlinear. The analysis based on the small-gain theorem is suitable for nonlinear systems since it only requires the highest gain value. In this case, when $P_{\text{gen}} = 0$, the highest gain is $I_{\text{sat}}/V_{\text{satL}}$, which is obtained when the phase voltage $V_x = V_{\text{satL}}$; see Fig. 1. However, when $P_{\text{gen}} > 0$ and the current limitation is activated, then the highest gain increases to $I_{\text{rated}}/V_{\text{satL}}$. Therefore, the stability condition is written as

$$\sqrt{(R_g)^2 + (\omega_g L_g)^2}\,\frac{I_{\text{rated}}}{V_{\text{satL}}} < 1. \tag{26}$$

Note that the proposed control does not have parameters to be designed, as it can be seen in (7)–(9), (11), and (16)–(19). As a consequence, the stability condition depends on the inverter (I_{rated}), the grid code (V_{satL}), and the grid impedance (R_g and $\omega_g L_g$).

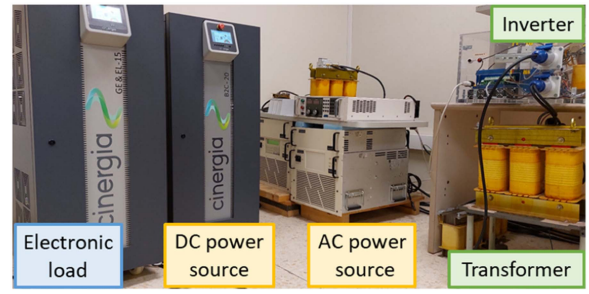

Fig. 5. Photograph of the experimental setup.

TABLE III
Nominal Values of the Laboratory Prototype

Quantity	Symbol	Nominal value
amplitude of the grid voltage	V_g	$110\sqrt{2}$ V (1 p. u.)
sag 1: positive-sequence voltage	V_{g1}^+	54.4 V (0.35 p. u.)
sag 1: negative-sequence voltage	V_{g1}^-	18.7 V (0.12 p. u.)
sag 1: phase between sequences	φ_1	70 °
sag 2: positive-sequence voltage	V_{g2}^+	140 V (0.90 p. u.)
sag 2: negative-sequence voltage	V_{g2}^-	62.2 V (0.40 p. u.)
sag 2: phase between sequences	φ_2	15 °
grid angular frequency	ω_g	$2\pi 60$ rad/s
grid resistance	R_g	0.1 Ω (0.006 p. u.)
grid inductance	L_g	4.8 mH (0.117 p. u.)
load resistance (full load)	R_L	22.8 Ω (1.471 p. u.)
load inductance (full load)	L_L	20 mH (0.486 p. u.)
transformer parasitic resistance	R_t	1.1 Ω (0.071 p. u.)
transformer parasitic inductance	L_t	0.6 mH (0.015 p. u.)
filter capacitor	C	1.3 μF (0.117 p. u.)
filter inductance	L	5.0 mH (0.122 p. u.)
rated inverter current amplitude	I_{rated}	10 A (1 p. u.)
sampling, switching frequency	f_s	10 kHz
dc-link voltage	V_{dc}	400 V
power source generation	P_{gen}	1 kW

V. Experimental Results

In this section, the experimental setup is first presented, then the operation of the proposed control is validated in several scenarios and, finally, a performance comparison with the controllers in Table I is reported.

A. Experimental Setup

The proposed control was tested in a laboratory setup based on the diagram, as shown in Fig. 2. A photograph of this setup is shown in Fig. 5. The hardware components were a Pacific Power AMX ac grid emulator (with a main and secondary modules), a Cinergia B2C-20 dc power source, a Cinergia GE and EL-15 ac electronic load, a Guasch BTL three-phase inverter, a transformer, and a Texas Instruments F28M36 digital-signal processor (DSP). The nominal values of the experimental setup are listed in Table III. The base voltage and current used to calculate per unit values are $V_{\text{base}} = V_g$ and $I_{\text{base}} = I_{\text{rated}}$. Note that two voltage sags were programmed in the grid emulator with

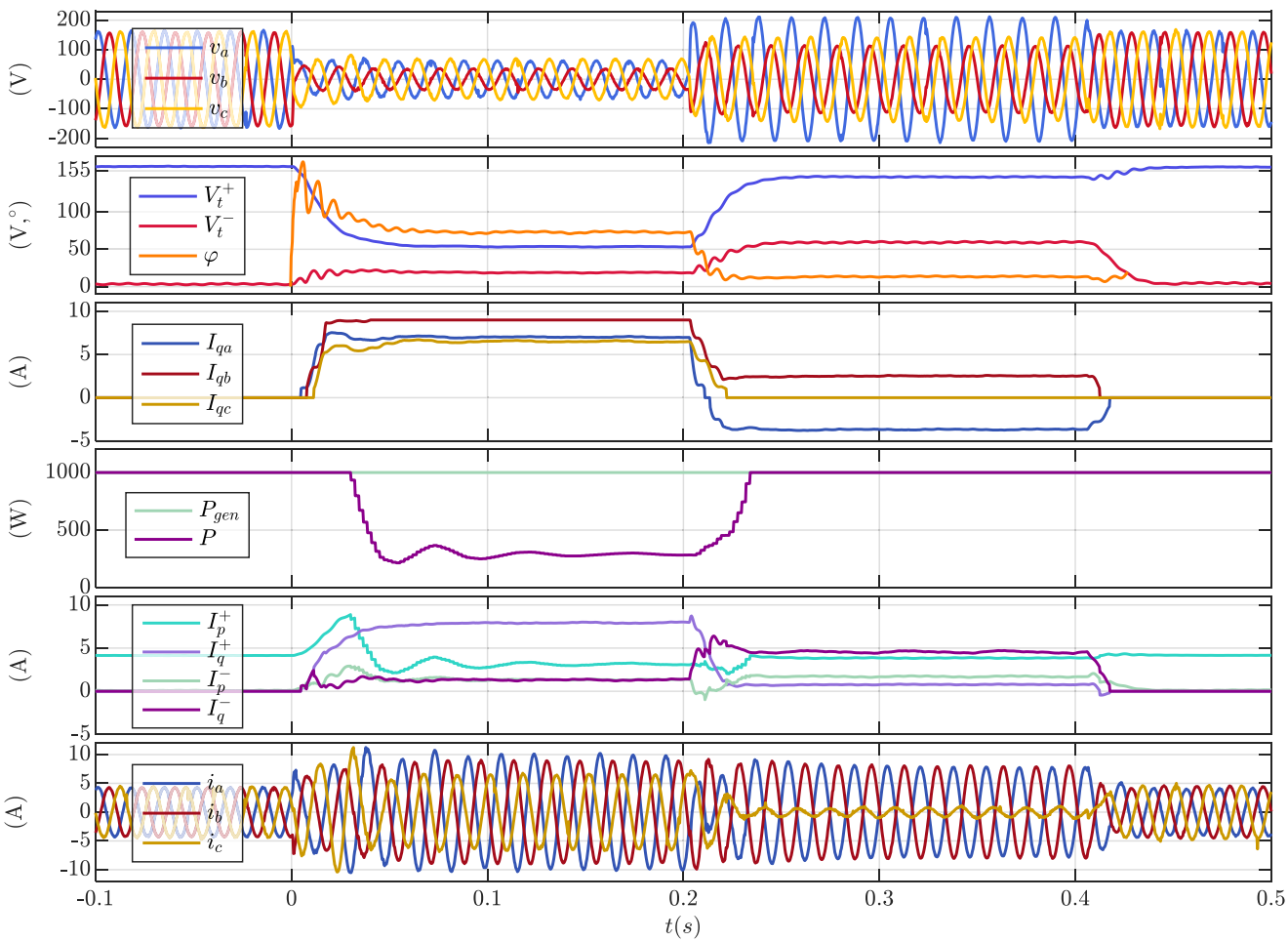

Fig. 6. Main waveforms of the proposed control during a complex grid fault composed by voltage sag 1 ($0 \leq t \leq 0.2$ s) and 2 (0.2 s $\leq t \leq 0.4$ s) when 10% of full load is supplied.

TABLE IV
NOMINAL VALUES OF THE GRID CODE IN FIG. 1

Quantity	Symbol	Nominal value
low saturation voltage	V_{satL}	0.25 p. u.
low dead band voltage	V_{dbL}	0.85 p. u.
high dead band voltage	V_{dbH}	1.10 p. u.
high saturation voltage	V_{satH}	1.75 p. u.
minimum reactive current	I_{qmin}	0.10 p. u.
saturation reactive current	I_{sat}	0.90 p. u.

low (sag 1) and high (sag 2) negative-sequence voltage. Table IV presents the nominal values of the grid code in Fig. 1. With these values, the proposed control is stable since the condition in (26) is met.

The proposed algorithm, as shown in Fig. 3, was programmed in the DSP. For the control strategies 1–4, the positive-sequence reactive current (I_q^+) is calculated, as shown in Table I. The rest of the sequence currents (I_p^+, I_p^-, I_q^-) are obtained using (23) and (25).

The computational load increase of the proposed control is less than 4.5% in the worst-case condition compared to that measured in controls 1–4. Therefore, the voltage support improvement illustrated in the following sections is obtained with a reduced increase in computational load.

B. Operation of the Proposed Control

This section presents the main waveforms to illustrate the operation of the proposed control. Details on voltage support are highlighted in the following sections.

Fig. 6 shows the main waveforms of the proposed control during a complex grid fault composed of voltage sags 1 and 2, when 10% of the full load is supplied. The experimental measurements were collected, sent from the DSP to a personal computer, and graphed with MATLAB, as shown in the figure. In subfigure 1 (from top to bottom), the waveforms are the phase voltages measured at the PCC. Note that the phase voltages programmed in the grid emulator have abrupt transitions between normal condition to sag 1 ($t = 0$ s), sag 1 to sag 2 ($t = 0.2$ s), and sag 2 to normal condition ($t = 0.4$ s). In subfigure 2, the waveforms are the outputs of the sequence voltage extractor,

which show slower dynamics compared with the phase voltages in subfigure 1. Much more interesting is to observe in subfigure 3 the values of the reactive phase currents, computed by (7). During voltage sag 1, these currents take close values because V_a, V_b, and V_c are similar (i.e., the negative-sequence voltage is low, as shown in subfigure 2). During voltage sag 2, the reactive phase currents are very different because V_a, V_b, and V_c are also very different (the negative-sequence voltage is high, as shown in subfigure 2). In particular, in phase b, the reactive current is positive, which produces an increase in V_b. In phase c, the reactive current is 0 since V_c voltage is in normal operation. In phase a, the reactive current is negative, producing a reduction in V_a. Therefore, as expected, each phase reacts differently from its measured voltage. This operating principle causes a clear improvement in voltage support, as shown in the following sections. Subfigure 4 shows the active powers. Since the dc power source was connected directly to the inverter, P denotes both the output power of this source and the input power of the inverter. In fact, in subfigure 4, P_{gen} is not a measured waveform. It is a constant value, included here to highlight the reduction in the active power of the inverter that occurs when the current tries to exceed I_{rated}, according to (11). It is worth mentioning that this reduction from 1 kW to 300 W does not affect the reactive phase currents, which continue performing their voltage support task correctly. Subfigure 5 shows the sequence currents, which were computed from (16)–(22). Note that I_p^+ is higher than I_p^- all the time. This is essential in the operation of the proposed control since the power source in Fig. 1 is unidirectional and cannot consume power. This issue is not important in the case of reactive currents because the reactive power is not consumed by the power source. In fact, in subfigure 5, I_Q^+ is higher than I_Q^- during sag 1, while I_Q^+ is lower than I_Q^- during sag 2. This does not represent any problem for the power source, which delivers positive active power during both sags (see subfigure 4). Finally, subfigure 6 shows the phase currents. During voltage sag 1, the current-limiting technique fixed the highest amplitude (phase a) to I_{rated} in steady state. Note that the attenuation of this amplitude does not introduce distortion in the current waveforms [25]. It is also interesting to observe that the current-limiting mechanism is not activated during voltage sag 2, resulting in phase currents with amplitudes lower than I_{rated} and an injected power of 1 kW.

C. Voltage Support

This section analyzes the impact of grid and load impedances on voltage support. The experimental study focuses on sag 2, where the overvoltage problem occurs; see Fig. 6.

In the first test, the nominal grid inductance was reduced from the nominal value of 4.8 mH (0.117 p.u.) to 3.2 mH (0.078 p.u.) and 1 mH (0.024 p.u.). The grid resistance is maintained approximately at 0.1 Ω (0.006 p.u.). Note that this test emulates the change from an initial weak grid to a final stiff grid, both with dominantly inductive behavior. Fig. 7(a) shows the measured voltage support in this test. As expected, voltage support improves as the grid inductance increases. This is because voltage support in an inductive grid is basically achieved through the injection of reactive current. Therefore, the higher

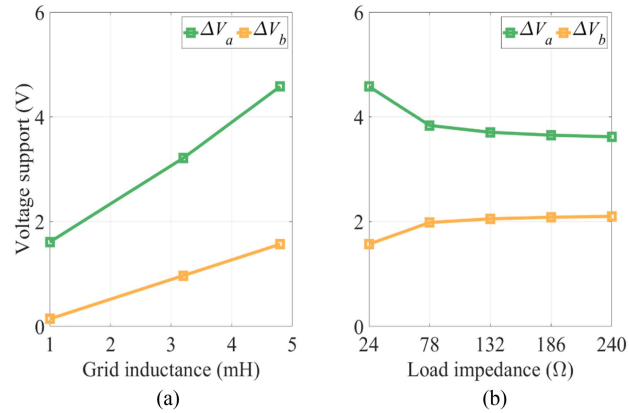

Fig. 7. Voltage support in sag 2 with different (a) grid inductances and (b) load impedances.

the inductance, the higher the voltage support (assuming that the reactive current remains constant). Two interesting issues observed in Fig. 7(a) are as follows: First, the voltage support is higher in phase a than in phase b. Therefore, thanks to the strategy proposed in (7), the current injection is concentrated in the phase where the overvoltage problem has occurred (see Fig. 6); second, the voltage of phase c is within the range $V_{\text{dbL}} < V < V_{\text{dbH}}$, so no reactive current injection occurs in this phase. According to (10), the voltage support is not defined in this case and, therefore, is not represented in this figure.

In the second test, the load impedance was reduced from full load (22.8 Ω and 20 mH) to 10% of full load (228 Ω and 200 mH). In this case, it is possible to identify two regions with different impacts on voltage support; see Fig. 7(b). In the right region (which includes values greater than approximately 78 Ω), the effect of the load impedance on the variations of V_a and V_b is negligible. This is because the power absorbed by the load in this region is small. In the left region, however, it is observed that the effect of load impedance is appreciable. The most interesting thing is that there is a clear improvement in voltage support in the phase where the overvoltage problem occurs. This is achieved by a slight worsening of the voltage support in the other faulty phase. In any case, the results obtained show that the impact of the grid impedance on voltage support is more important than the effect of the load impedance; compare Fig. 7(a) with Fig. 7(b).

D. Performance Comparison

Tables V and VI list the results measured during voltage sag 1 and 2, respectively, when testing the experimental setup with 10% of full load. It is worth mentioning that to compare performance, tests have also been carried out with other loading conditions, reaching the same conclusions that are drawn from the results presented in the following text. In both tables, the blue shaded columns show the voltage measurements. In dark blue, the voltages responsible for fixing the reactive positive-sequence current for controls 1–4 and the reactive phase currents for the proposed control are highlighted. The columns shaded in purple show the sequence currents. In dark purple, the currents fixed by the grid code in Fig. 1 are highlighted. Finally, the green

TABLE V
PERFORMANCE COMPARISON OF REACTIVE CURRENT INJECTION STRATEGIES DURING VOLTAGE SAG 1 (NO INJECTION: $V_{a,NI} = 0.399$ p.u., $V_{b,NI} = 0.236$ p.u., and $V_{c,NI} = 0.443$ p.u.)

Ctrl	V^+, p.u.	V_{ag}, p.u.	V_{ef}, p.u.	V_{min}, p.u.	V_a, p.u.	V_b, p.u.	V_c, p.u.	I_p^+, A	I_q^+, A	I_p^-, A	I_q^-, A	ΔV_a, %	ΔV_b, %	ΔV_c, %
1	0.443	–	–	–	0.472	0.340	0.547	6.41	6.42	0	0	18.3	44.1	23.5
2	–	0.452	–	–	0.470	0.339	0.546	6.56	6.30	0	0	17.8	43.6	23.2
3	–	–	0.463	–	0.468	0.338	0.545	6.72	6.16	0	0	17.3	43.2	23.0
4	–	–	–	0.350	0.497	0.350	0.559	4.35	7.66	0	0	24.6	48.3	26.2
prop.	–	–	–	–	0.493	0.354	0.513	3.14	7.94	1.37	1.30	23.6	50.1	15.8

TABLE VI
PERFORMANCE COMPARISON OF REACTIVE CURRENT INJECTION STRATEGIES DURING VOLTAGE SAG 2 (NO INJECTION: $V_{a,NI} = 1.297$ p.u., $V_{b,NI} = 0.713$ p.u., and $V_{c,NI} = 0.852$ p.u.)

Ctrl	V^+, p.u.	V_{ag}, p.u.	V_{ef}, p.u.	V_{min}, p.u.	V_a, p.u.	V_b, p.u.	V_c, p.u.	I_p^+, A	I_q^+, A	I_p^-, A	I_q^-, A	ΔV_a, %	ΔV_b, %	ΔV_c, %
1	0.900	–	–	–	1.295	0.690	0.877	4.78	0	0	0	0.15	−3.23	–
2	–	0.954	–	–	1.295	0.690	0.877	4.78	0	0	0	0.15	−3.23	–
3	–	–	0.990	–	1.295	0.690	0.877	4.78	0	0	0	0.15	−3.23	–
4	–	–	–	0.723	1.329	0.723	0.906	4.78	2.69	0	0	−2.49	1.40	–
prop.	–	–	–	–	1.250	0.728	0.862	3.85	0.73	1.70	4.56	3.62	2.10	–

shaded columns show the merit factors for voltage support. The cells shaded in dark green or red are highlighted to compare the performance of the proposed control. These last results are discussed in detail in the following text.

Focusing on Table V, note that all the voltages shaded in dark blue are below $V_{\mathrm{dbL}} = 0.85$ p.u. Therefore, the reactive currents shaded in dark purple are higher than 0. In particular, the voltages for controls 1–3 are very similar so that the results obtained for voltage support are also very similar. In control 4, the voltage is lower than in controls 1–3, resulting in both higher reactive positive-sequence current and a clear improvement in voltage support. In the proposed control, the results in this scenario with low negative-sequence voltage are similar to those measured in control 4. However, it is worth noting the independent injection per phase in the proposed control, which causes a greater improvement in the phase with lower voltage (see the results in phase b). The phase with the highest voltage (phase c) is the one with lowest priority, so the improvement in voltage support is less than in the other phases. Finally, in the phase with intermediate voltage (phase a), the improvement in voltage support is practically the same as in control 4. In short, the measured results show that the proposed control prioritizes the voltage support in the phase with lowest amplitude when the voltages are lower than V_{dbL}. This operating principle guarantees the best voltage support in this scenario.

In Table VI, the voltage in phase c is in normal operation, so the merit factor ΔV_c is not considered; see the definition in (10). For controls 1–3, the dark blue shaded voltages are also in normal operation, so no reactive current injection is performed. In this case, the voltage in phase b is slightly reduced by the active current injection, causing a negative value in ΔV_b. For control 4, the dark blue shaded voltage is below V_{dbL}, what results in an injection of reactive positive-sequence current. This current increases the voltage on all three phases simultaneously, producing an overvoltage problem in phase a. In this case, the problem is quantified as a voltage increase of 2.49% (see the text shaded in dark red for control 4). The proposed control solves this problem. The individual injection of reactive current makes the action on the voltages independent for each phase. In this way, the voltage in phase a is reduced, while the voltage in phase b is increased. This operating principle produces a positive merit factor for voltage support, as shown in dark green in the table. Actually, the percentages of voltage support improvement are lower in voltage sag 2 compared with voltage sag 1. This is because the voltages in voltage sag 2 are closer to the normal operation. In any case, the relevance of the proposed control lies in the independent action in each phase, which allows to improve the phase voltages in any situation.

VI. CONCLUSION

In this article, a control scheme to solve overvoltage problems in three-phase three-wire power inverters had been proposed. In three-wire inverters, this is a really challenging problem because the phase voltages are coupled. The control is based on the injection of reactive current for each phase independently. The solved mathematical problem (i.e., the theoretical contribution of this study) has consisted in mapping the reactive phase currents and the active power in the active and reactive sequence currents of the inverter. This mapping had not been previously presented in the literature. From a practical point-of-view, the control scheme has also included a current-limiting technique to set the maximum amplitude of the phase currents to the rated current in overcurrent conditions. The experimental results measured from a laboratory prototype have made it possible to compare the performance of the proposed control with those obtained with various state-of-the-art control techniques. This study validated the superiority of the proposed control in overvoltage situations. Specifically, in these critical situations, the proposed control reduces the voltage of the phases above

V_{dbH}, increases the voltage of the phases below V_{dbL}, and does not affect the voltage of the phases that operate in normal mode. All these properties are achieved in safe current conditions by limiting the maximum current when needed. In addition, these properties are maintained for different impedance values of the local load. As a final remark, the computational load of the proposed control has been increased by less than 4.5% in the worst-case condition compared with the results obtained with the state-of-the-art control solutions.

The most appropriate application scenario of the proposed control has also been identified in this article. In fact, the experimental results show that the voltage support in stiff grids with small line impedances is very limited, so reactive current injection strategies (including the proposed one) have little impact. Therefore, the proposed control is relevant in weak grids with medium to high line impedances.

Appendix

The active and reactive (phase) powers, as expressed in Table II, are derived as follows.

The definition of the instantaneous active and reactive phase powers in a natural reference frame is [20], [25]

$$p = v_{ta}\, i_a + v_{tb} i_b + v_{tc} i_c \tag{A1}$$

$$q_a = v_{ta}^{\perp}\, i_a \tag{A2}$$

$$q_b = v_{tb}^{\perp}\, i_b \tag{A3}$$

$$q_c = v_{tc}^{\perp}\, i_c \tag{A4}$$

where $v_{tx}^{\perp}$ denotes the quadrature voltage of v_{tx}. In systems with unbalanced voltage, these powers include oscillating terms with zero mean value. These terms are not considered in this analysis.

In a stationary reference frame, voltages and their quadrature components can be written as [26]

$$v_{t\alpha} = V_t^{+} \cos(\omega t) + V_t^{-} \cos(\omega t + \varphi) \tag{A5}$$

$$v_{t\beta} = V_t^{+} \sin(\omega t) - V_t^{-} \sin(\omega t + \varphi) \tag{A6}$$

$$v_{t\alpha}^{\perp} = V_t^{+} \sin(\omega t) + V_t^{-} \sin(\omega t + \varphi) \tag{A7}$$

$$v_{t\beta}^{\perp} = -V_t^{+} \cos(\omega t) + V_t^{-} \cos(\omega t + \varphi)\,. \tag{A8}$$

Assuming that the current control loop is correctly tuned [45], the $\alpha\beta$ currents are written from (1) and (2) as

$$i_\alpha = i_{p\alpha} + i_{q\alpha} \tag{A9}$$

$$i_\beta = i_{p\beta} + i_{q\beta} \tag{A10}$$

where

$$i_{p\alpha} = I_p^{+} \cos(\omega t) + I_p^{-} \cos(\omega t + \varphi) \tag{A11}$$

$$i_{p\beta} = I_p^{+} \sin(\omega t) - I_p^{-} \sin(\omega t + \varphi) \tag{A12}$$

$$i_{q\alpha} = I_q^{+} \sin(\omega t) + I_q^{-} \sin(\omega t + \varphi) \tag{A13}$$

$$i_{q\beta} = -I_q^{+} \cos(\omega t) + I_q^{-} \cos(\omega t + \varphi)\,. \tag{A14}$$

The next step is to convert the $\alpha\beta$ variables in (A5)–(A14) to abc components using the inverse Clarke transformation. Finally, the powers in Table II are obtained by inserting the abc voltages and currents in (A1)–(A4).

References

[1] P. Heine, P. Pohjanheimo, M. Lehtonen, and E. Lakervi, "A method for estimating the frequency and cost of voltage sags," *IEEE Trans. Power Syst.*, vol. 17, no. 2, pp. 290–296, May 2002.

[2] L. Zhan and M. H. J. Bollen, "Characteristic of voltage dips (sags) in power systems," *IEEE Trans. Power Del.*, vol. 15, no. 2, pp. 827–832, Apr. 2000.

[3] M. H. J. Bollen, "Voltage recovery after unbalanced and balanced voltage dips in three-phase systems," *IEEE Trans. Power Del.*, vol. 18, no. 4, pp. 1376–1381, Oct. 2003.

[4] G. S. Chawda, A. G. Shaik, O. P. Mahela, S. Padmanaban, and J. B. Holm-Nielsen, "Comprehensive review of distributed FACTS control algorithms for power quality enhancement in utility grid with renewable energy penetration," *IEEE Access*, vol. 8, pp. 107614–107634, 2020.

[5] A. Mishra and K. Chatterjee, "Flicker attenuation using FACTS device for DFIG-based WECS connected to distribution network," *IEEE Syst. J.*, vol. 17, no. 1, pp. 282–293, Mar. 2023.

[6] S. D. Swain, P. K. Ray, and K. B. Mohanty, "Improvement of power quality using a robust hybrid series active power filter," *IEEE Trans. Power Electron.*, vol. 32, no. 5, pp. 3490–3498, May 2017.

[7] P. Salmeron and S. P. Litran, "Improvement of the electric power quality using series active and shunt passive filters," *IEEE Trans. Power Del.*, vol. 25, no. 2, pp. 1058–1067, Apr. 2010.

[8] G. Kou et al., "Load rejection overvoltage of utility-scale distributed solar generation," *IEEE Trans. Power Del.*, vol. 35, no. 4, pp. 2113–2116, Aug. 2020.

[9] S. N. Salih and P. Chen, "On coordinated control of OLTC and reactive power compensation for voltage regulation in distribution systems with wind power," *IEEE Trans. Power Syst.*, vol. 31, no. 5, pp. 4026–4035, Sep. 2016.

[10] C. Lin, W. Wu, B. Zhang, B. Wang, W. Zheng, and Z. Li, "Decentralized reactive power optimization method for transmission and distribution networks accommodating large-scale DG integration," *IEEE Trans. Sustain. Energy*, vol. 8, no. 1, pp. 363–373, Jan. 2017.

[11] T. Q. Fonsêca, R. L. A. Ribeiro, T. de Oliveira Alves Rocha, F. B. Costa, and J. M. Guerrero, "Voltage grid supporting by using variable structure adaptive virtual impedance for LCL-voltage source converter DG converters," *IEEE Trans. Ind. Electron.*, vol. 67, no. 11, pp. 9326–9336, Nov. 2020.

[12] D. Moutevelis, J. Roldan-Perez, N. Jankovic, and M. Prodanovic, "Recursive secondary controller for voltage profile improvement based on primary virtual admittance control," *IEEE Trans. Smart Grid*, vol. 14, no. 6, pp. 4296–4311, Nov. 2023.

[13] A. S. Vijay, S. Doolla, and M. C. Chandorkar, "Varying negative sequence virtual impedance adaptively for enhanced unbalanced power sharing among DGs in islanded AC microgrids," *IEEE Trans. Energy Convers.*, vol. 36, no. 4, pp. 3271–3281, Dec. 2021.

[14] S. Maganti and N. P. Padhy, "A feedback-based flexible compensation strategy for a weak-grid-tied current-controlled converter under unbalanced and harmonic conditions," *IEEE Trans. Ind. Appl.*, vol. 58, no. 6, pp. 7739–7753, Nov./Dec. 2022.

[15] Á. Borrell, M. Velasco, A. Camacho, J. Miret, and M. Castilla, "Remote negative-sequence voltage fair compensation in grid-forming inverter-based islanded AC microgrids," *IEEE Trans. Power Electron.*, vol. 38, no. 10, pp. 12570–12582, Oct. 2023.

[16] M. Altin, O. Goksu, R. Teodorescu, P. Rodriguez, B. Bak-Jensen, and L. Helle, "Overview of recent grid codes for wind power integration," in *Proc. IEEE 12th Int. Conf. Optim. Elect. Electron. Equip.*, 2010, pp. 1152–1160.

[17] M. Tsili and S. Papathanassiou, "A review of grid code technical requirements for wind farms," *IET Renewable Power Gener.*, vol. 3, no. 3, pp. 308–332, Sep. 2009.

[18] "P.O.12.3—Response requirements against voltage dips in wind installations," *Red Eléctrica de España (REE), Grid Code*, Alcobendas, Spain, Oct. 2006.

[19] "P.O.12.2—Connected installations to the transmission Spanish system: Minimum requirements for design and security—Grid code requirements for installations connected to the transmission system in Spain," *Red Eléctrica España (REE), Grid Code*, Alcobendas, Spain, 2012.

[20] *IEEE Standard for Interconnection and Interoperability of Distributed Energy Resources With Associated Electric Power Systems Interfaces*, *IEEE Standard 1547-2018*, Apr. 2018, pp. 1–138.

[21] "Technical requirements for the connection of generating stations to the hydro-québec transmission system," *Hydro Québec TransÉnergie, Grid Code*, Montreal, QC, Canada, Jan. 2019.
[22] "Implementation guideline for network code: Requirements for grid connection applicable to all generators," *Eur. Netw. Transmiss. Syst. Oper. Electricity*, Brussels, Belgium, Tech. Rep. 1, Oct. 2013.
[23] "Summary of the draft VDE-AR-N 4120:2017-05," *VDE, Grid Code*, Frankfurt, Germany, May 2017.
[24] *IEEE Draft Standard for Interconnection and Interoperability of Inverter Based Resources (IBR) Interconnecting With Associated Transmission Electric Power Systems*, *IEEE Standard P2800/D6.0*, Mar. 2021, pp. 1–170.
[25] J. Jia, G. Yang, and A. H. Nielsen, "A review on grid-connected converter control for short-circuit power provision under grid unbalanced faults," *IEEE Trans. Power Del.*, vol. 33, no. 2, pp. 649–661, Apr. 2018.
[26] J. Joshi, A. K. Swami, V. Jately, and B. Azzopardi, "A comprehensive review of control strategies to overcome challenges during LVRT in PV systems," *IEEE Access*, vol. 9, pp. 121804–121834, 2021.
[27] F. Wang, J. L. Duarte, and M. A. M. Hendrix, "Pliant active and reactive power control for grid-interactive converters under unbalanced voltage dips," *IEEE Trans. Power Electron.*, vol. 26, no. 5, pp. 1511–1521, May 2011.
[28] A. Milicua, G. Abad, and M. A. R. Vidal, "Online reference limitation method of shunt-connected converters to the grid to avoid exceeding voltage and current limits under unbalanced operation—Part I: Theory," *IEEE Trans. Energy Convers.*, vol. 30, no. 3, pp. 852–863, Sep. 2015.
[29] O. Goksu, R. Teodorescu, C. L. Bak, F. Iov, and P. C. Kjær, "Impact of wind power plant reactive current injection during asymmetrical grid faults," *IET Renewable Power Gener.*, vol. 7, no. 5, pp. 484–492, Sep. 2013.
[30] C. Nithya and J. P. Roselyn, "Multimode inverter control strategy for LVRT and HVRT capability enhancement in grid connected solar PV system," *IEEE Access*, vol. 10, pp. 54899–54911, 2022.
[31] S. Alepuz et al., "Control strategies based on symmetrical components for grid-connected converters under voltage dips," *IEEE Trans. Ind. Electron.*, vol. 56, no. 6, pp. 2162–2173, Jun. 2009.
[32] A. Azizi, A. Banaiemoqadam, A. Hooshyar, and M. Patel, "A blind spot in the LVRT current requirements of modern grid codes for inverter-based resources," *IEEE Trans. Power Del.*, vol. 38, no. 1, pp. 319–334, Feb. 2023.
[33] S. K. Chaudhary, R. Teodorescu, P. Rodriguez, P. C. Kjær, and A. M. Gole, "Negative sequence current control in wind power plants with VSC-HVDC connection," *IEEE Trans. Sustain. Energy*, vol. 3, no. 3, pp. 535–544, Jul. 2012.
[34] H.-S. Song and K. Nam, "Dual current control scheme for PWM converter under unbalanced input voltage conditions," *IEEE Trans. Ind. Electron.*, vol. 46, no. 5, pp. 953–959, Oct. 1999.
[35] T.-L. Lee, S.-H. Hu, and Y.-H. Chan, "D-STATCOM with positive-sequence admittance and negative-sequence conductance to mitigate voltage fluctuations in high-level penetration of distributed-generation systems," *IEEE Trans. Ind. Electron.*, vol. 60, no. 4, pp. 1417–1428, Apr. 2013.
[36] P. Rodriguez, A. Timbus, R. Teodorescu, M. Liserre, and F. Blaabjerg, "Reactive power control for improving wind turbine system behavior under grid faults," *IEEE Trans. Power Electron.*, vol. 24, no. 7, pp. 1798–1801, Jul. 2009.
[37] J. A. Suul, A. Luna, P. Rodriguez, and T. Undeland, "Virtual-flux-based voltage-sensor-less power control for unbalanced grid conditions," *IEEE Trans. Power Electron.*, vol. 27, no. 9, pp. 4071–4087, Sep. 2012.
[38] *IEEE Standard Definitions for the Measurement of Electric Power Quantities Under Sinusoidal, Nonsinusoidal, Balanced, or Unbalanced Conditions*, *IEEE Standard 1459-2010*, Mar. 2010, pp. 1–40.
[39] A. Camacho, M. Castilla, J. Miret, L. García de Vicuna, and G. L. M. Andres, "Control strategy for distribution generation inverters to maximize the voltage support in the lowest phase during voltage sags," *IEEE Trans. Ind. Electron.*, vol. 65, no. 3, pp. 2346–2355, Mar. 2018.
[40] M. Mirhosseini, J. Pou, and V. G. Agelidis, "Individual phase current control with the capability to avoid overvoltage in grid-connected photovoltaic power plants under unbalanced voltage sags," *IEEE Trans. Power Electron.*, vol. 30, no. 10, pp. 5346–5351, Oct. 2015.
[41] K. Ma, W. Chen, M. Liserre, and F. Blaabjerg, "Power controllability of a three-phase converter with an unbalanced AC source," *IEEE Trans. Power Electron.*, vol. 30, no. 3, pp. 1591–1604, Mar. 2015.
[42] P. Rodriguez, A. Luna, I. Candela, R. Mujal, R. Teodorescu, and F. Blaabjerg, "Multiresonant frequency-locked loop for grid synchronization of power converters under distorted grid conditions," *IEEE Trans. Ind. Electron.*, vol. 58, no. 1, pp. 127–138, Jan. 2011.
[43] F. J. Rodriguez, E. Bueno, M. Aredes, L. G. B. Rolim, F. A. S. Neves, and M. C. Cavalcanti, "Discrete-time implementation of second order generalized integrators for grid converters," in *Proc. IEEE 34th Annu. Conf. IEEE Ind. Electron.*, 2008, pp. 176–181.
[44] M. Garnica, L. García de Vicuna, J. Miret, M. Castilla, and R. Guzmán, "Optimal voltage-support control for distributed generation inverters in RL grid-faulty networks," *IEEE Trans. Ind. Electron.*, vol. 67, no. 10, pp. 8405–8415, Oct. 2020.
[45] J. Rocabert, A. Luna, F. Blaabjerg, and P. Rodriguez, "Control of power converters in AC microgrids," *IEEE Trans. Power Electron.*, vol. 27, no. 11, pp. 4734–4749, Nov. 2012.
[46] Q. Zhang, J. He, Y. Xu, Z. Hong, Y. Chen, and K. Strunz, "Average-value modeling of direct-driven PMSG-based wind energy conversion systems," *IEEE Trans. Energy Convers.*, vol. 37, no. 1, pp. 264–273, Mar. 2022.
[47] F. Ahmadloo and S. P. Azad, "Analysis of internal control loop interactions in VSCs: An individual design perspective," *IEEE Trans. Power Del.*, vol. 37, no. 3, pp. 1465–1475, Jun. 2022.
[48] P. Verma, M. N. Anwar, M. K. Ram, and A. Iqbal, "Internal model control scheme-based voltage and current mode control of DC-DC boost converter," *IEEE Access*, vol. 11, pp. 110558–110569, 2023.
[49] M. Castilla, J. Miret, A. Camacho, L. García de Vicuna, and J. Matas, "Modeling and design of voltage support control schemes for three-phase inverters operating under unbalanced grid conditions," *IEEE Trans. Power Electron.*, vol. 29, no. 11, pp. 6139–6150, Nov. 2014.

José Ignacio Iñiguez received the B.S. degree in industrial electronic engineering and the M.S. degree in automation and industrial electronics from the Universitat Politècnica de Catalunya, Barcelona, Spain, in 2016 and 2020, respectively.

His research interests include dc/dc and dc/ac converter, control systems, and power electronics.

Josué Neftali Duarte was born in Catacamas, Honduras. He received the B.S. degree in mechatronic engineering from the Universidad Tecnológica Centroamericana, Tegucigalpa, Honduras, in 2018, and the M.S. degree in automatic systems and industrial electronics engineering in 2021 from the Universitat Politècnica de Catalunya, Barcelona, Spain, where he is currently working toward the Ph.D. degree in automatic control, robotics and computer vision with the Department of Automatic Control.

His current research interests include power electronics, control systems, and microgrids.

Antonio Camacho received the B.S. degree in chemical engineering, the M.S. degree in automation and industrial electronics, and the Ph.D. degree in electronic engineering from the Universitat Politècnica de Catalunya, Barcelona, Spain, in 2000, 2009, and 2015, respectively.

His research interests include networked and embedded control systems, industrial informatics, and power electronics.

Jaume Miret (Member, IEEE) received the B.S. degree in telecommunications, the M.S. degree in electronics, and the Ph.D. degree in electronics from the Universitat Politècnica de Catalunya, Barcelona, Spain, in 1992, 1999, and 2005, respectively.

From 1993 to 2011, he was an Assistant Professor with the Department of Electronic Engineering, Universitat Politècnica de Catalunya, where he has been an Associate Professor since 2011, and teaches courses on digital design and circuit theory. His research interests include dc-to-ac converters, active power filters, and digital control.

Miguel Castilla received the B.S., M.S., and Ph.D. degrees in telecommunication engineering from the Universitat Politècnica de Catalunya, Barcelona, Spain, in 1988, 1995, and 1998, respectively.

Since 2019, he has been a Full Professor with the Department of Electronic Engineering, Universitat Politècnica de Catalunya, where he teaches courses on control of power electronics' converters and systems. His research interests include power electronics, control, renewable energy systems, and electrical microgrids.